remote sensing

MDPI

Article

Overview and Analysis of Ground Subsidence along China's Urban Subway Network Based on Synthetic Aperture Radar Interferometry

Shunyao Wang [1,2,3], Zhenwei Chen [4,*], Guo Zhang [4], Zixing Xu [4], Yutao Liu [4] and Yuan Yuan [5]

[1] School of Geographic Science and Tourism, Nanyang Normal University, Nanyang 473000, China; shunyaowang@whu.edu.cn
[2] Key Laboratory of Natural Disaster and Remote Sensing of Henan Province, Nanyang Normal University, Nanyang 473000, China
[3] Engineering Research Center of Environmental Laser Remote Sensing Technology and Application of Henan Province, Nanyang Normal University, Nanyang 473000, China
[4] State Key Laboratory of Information Engineering in Surveying, Mapping and Remote Sensing, Wuhan University, Wuhan 430000, China; guozhang@whu.edu.cn (G.Z.); zixingxu@whu.edu.cn (Z.X.); yutaoliu@whu.edu.cn (Y.L.)
[5] School of Computer, Wuhan University, Wuhan 430000, China; yuany@whu.edu.cn
* Correspondence: guanyuechen@whu.edu.cn

Abstract: Deformation along a subway rail network is related to the safe operation of the subway and the stability of construction facilities on the surface, making long-term deformation monitoring imperative. Long-term monitoring of surface deformation along the subway network and statistical analysis of the overall deformation situation are lacking in China. Therefore, targeting 35 Chinese cities whose subway mileage exceeds 50 km, we extracted their surface deformation along subway networks between 2018 and 2022, using spaceborne synthetic aperture radar (SAR) interferometry (InSAR) technology and Sentinel-1 satellite data. We verified the results with the continuous global navigation satellite system (GNSS) stations' data and found that the root mean square error (RMSE) of the InSAR results was 3.75 mm/year. Statistical analysis showed that ground subsidence along the subways was more prominent in Beijing, Tianjin, and other areas in the North China Plain, namely Kunming (which is dominated by karst landforms), as well as Shanghai, Guangzhou, Qingdao, and other coastal cities. In addition, an analysis revealed that the severity of surface subsidence correlated positively with a city's gross domestic product (GDP) with a Pearson correlation of 0.787, since the higher the GDP, the more frequent the construction and maintenance of subway, and the more commuters there are, which in turn exacerbates the disturbance to the surface. Additionally, the type of land cover also affects the ground deformation. Our findings provide a reference for constructing, operating, and maintaining the urban subway systems in China.

Keywords: China; ground deformation; subsidence; subway; synthetic aperture radar interferometry

check for updates

Citation: Wang, S.; Chen, Z.; Zhang, G.; Xu, Z.; Liu, Y.; Yuan, Y. Overview and Analysis of Ground Subsidence along China's Urban Subway Network Based on Synthetic Aperture Radar Interferometry. *Remote Sens.* **2024**, *16*, 1548. https://doi.org/10.3390/rs16091548

Academic Editors: Mohammad Omidalizarandi, Mozhdeh Shahbazi and Mohammad Ali Sharifi

Received: 23 March 2024
Revised: 23 April 2024
Accepted: 24 April 2024
Published: 26 April 2024

Copyright: © 2024 by the authors. Licensee MDPI, Basel, Switzerland. This article is an open access article distributed under the terms and conditions of the Creative Commons Attribution (CC BY) license (https://creativecommons.org/licenses/by/4.0/).

1. Introduction

With relentless urbanization and exponential population growth, urban aboveground transportation infrastructures are reaching their saturation point and becoming increasingly overwhelmed. In order to ease the strain on surface-level transportation facilities, large and medium-sized cities have turned their attention towards underground spaces, embarking on the development of subway networks [1,2]. As of December 2020, 47 cities in China had established subway systems, boasting 208 operational lines and a total length of 6730.27 km [3]. Subway networks enhance the convenience of travel, yet also serve as crucial infrastructure for the survival and sustained development of urban centers [4].

Ground disturbances are inevitable during construction and, in particular, during the operation of a subway, leading to surface deformation, which may further induce cracking

in surrounding buildings, pipeline breakage, and road collapse [5–7]. China has seen numerous instances of surface subsidence in cities during subway construction and operation [8,9]. Given that urban subway networks are typically situated in densely populated and highly congested areas, the consequences of such incidents can be particularly severe. To effectively prevent and mitigate disasters and accidents caused by subway construction and operation, it is imperative to undertake extensive and continuous monitoring of surface deformation along subway networks.

Although traditional monitoring methods, such as levelling and deformation gauges, offer high accuracy when focused on single targets, their coverage remains limited [10]. Furthermore, deploying real-time monitoring equipment comes with significant financial implications. However, the advancement of aerospace technology has given rise to an increasing diversity of Earth observation methods [11]. Among them, synthetic aperture radar interferometry (InSAR) stands out as a prominent measurement technology [12–16]. InSAR's vast coverage, precision, and active imaging capabilities have opened new horizons in terrain mapping, as well as the study of urban deformation, volcanic activity, glacier movements, earthquakes, energy resources, and numerous other applications [17–20].

In recent years, InSAR technology has proven its worth in monitoring urban subway deformation, leading to several successful applications. Scholars have conducted targeted InSAR monitoring of subway deformation in several major cities, such as Seoul [21], Manila [22], Bucharest [23], Beijing [8,24], Shanghai [25–27], Urumqi [28], Suzhou [29], Qingdao [30], Xuzhou [31], Chengdu [32], Nanchang [33], and Hohhot [34]. These applications have effectively demonstrated the effectiveness of InSAR in monitoring subway deformation. However, these efforts have primarily been limited to individual cities, and the academic community has yet to conduct regional-scale surveys, integrated analyses, and explorations of deformation patterns for subway systems across a wide area. In view of these advancements, we aimed to use InSAR technology to extract surface deformation data along the subway networks of major cities in China from 2018 to 2022 and to analyze the surface deformation patterns of Chinese cities with subway systems, providing valuable insights for subway planning and operations.

2. Materials and Methods

2.1. Study Area and Data

By the end of 2022, nearly 50 cities in China had established subways, but only 35 of them had operational mileages exceeding 50 km [35]. To ensure the representativeness of our research, we excluded cities with subway mileages shorter than 50 km from our analysis. Consequently, we focused our study on the subway networks of 35 cities, whose details are outlined in Table 1. The geographical distribution of these cities is depicted in Figure 1.

Table 1. Detailed subway and SAR data information.

No.	City	Operation		Sentinel Identifier		Number of Acquisitions	Direction	Incidence Angle (Degree)
		Lines	Mileage (km)	Path	Frame			
1	Beijing	27	797.3	142	126	146	Ascending	39.42
2	Shanghai	20	825.0	171	96	145	Ascending	39.60
3	Guangzhou	16	609.8	11	71	148	Ascending	39.67
4	Shenzhen	16	558.6	11 11	65 71	148 148	Ascending	39.71 39.67
5	Chengdu	13	557.8	128	94	147	Ascending	39.63
6	Hangzhou	12	516.0	69	94	141	Ascending	39.63
7	Wuhan	11	504.3	113	96	125	Ascending	39.64
8	Nanjing	12	448.8	69	99	139	Ascending	39.60
9	Chongqing	11	434.6	55	92	134	Ascending	39.59
10	Qingdao	7	323.8	171 171	111 116	143 143	Ascending	39.52 39.48

Table 1. *Cont.*

No.	City	Operation		Sentinel Identifier		Number of Acquisitions	Direction	Incidence Angle (Degree)
		Lines	Mileage (km)	Path	Frame			
11	Tianjin	8	286.0	69	124	133	Ascending	39.20
12	Xi'an	8	272.4	84 84	105 110	138 138	Ascending	39.55 39.52
13	Suzhou	5	254.2	69	99	139	Ascending	39.60
14	Hongkong	10	245.3	11	65	148	Ascending	39.71
15	Zhengzhou	8	233.0	113 113	106 111	125 119	Ascending	39.62 39.59
16	Dalian	5	212.6	98	124	140	Ascending	39.45
17	Changsha	7	209.1	11	86	137	Ascending	39.60
18	Ningbo	5	186.0	171	91	145	Ascending	39.63
19	Hefei	5	168.8	142	101	147	Ascending	39.58
20	Kunming	6	165.9	26	78	148	Ascending	39.65
21	Nanchang	4	128.5	40	87	148	Ascending	39.65
22	Nanning	5	128.2	157	67	148	Ascending	39.70
23	Foshan	4	127.3	11	71	148	Ascending	39.67
24	Shenyang	4	117.1	3	455	90	Descending	39.60
25	Wuxi	4	110.8	69	99	139	Ascending	39.60
26	Fuzhou	4	110.7	142	81	146	Ascending	39.67
27	Changchun	5	106.7	105	446	121	Descending	39.60
28	Xiamen	3	98.4	142	75	146	Ascending	39.69
29	Jinan	3	84.1	142	116	147	Ascending	39.48
30	Harbin	3	78.1	105	441	118	Descending	39.58
31	Guiyang	2	74.4	55	82	136	Ascending	39.63
32	Shijiazhuang	3	74.3	40	122	148	Ascending	39.45
33	Xuzhou	3	64.1	142	106	147	Ascending	39.55
34	Changzhou	2	54.0	69	99	139	Ascending	39.60
35	Wenzhou	1	52.5	69 69	84 89	140 141	Ascending	39.67 39.65

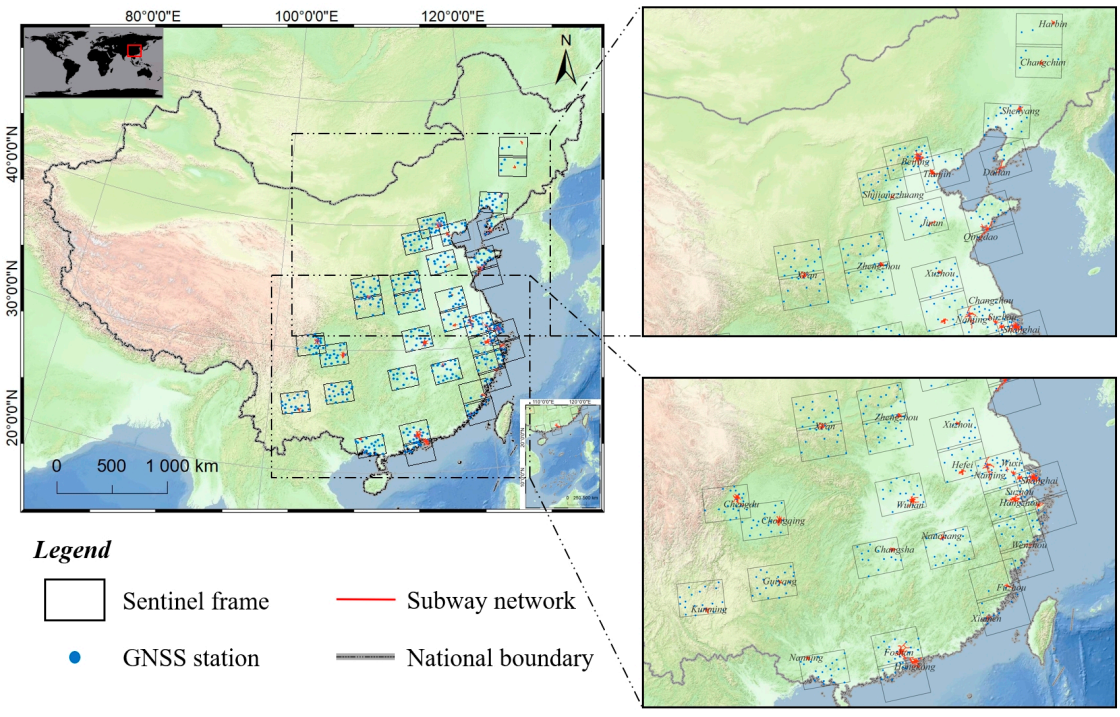

Figure 1. Study area and data coverage.

The SAR data analyzed in this study were all in Sentinel-1 interferometric wide mode. We needed 34 frames to cover the subway networks of all 35 cities of interest, as some cities required two frames to cover the network. The SAR data timespan ranged from early 2018 to the end of 2022, and the data acquisition interval was in most cases 12 days. However, due to factors such as temporary satellite maneuvers, data for some periods are missing. Table 1 shows the final details of the data used for each city, with 34 frames and 4705 acquisitions. To validate the accuracy of the subsequent InSAR results, we also collected data from 465 evenly distributed continuous GNSS stations as the ground truth.

2.2. SBAS-InSAR Workflow

Owing to the large expanse of subway networks and the enormous amount of data involved, we adopted the small baseline subset InSAR (SBAS-InSAR) method to extract surface deformation [36]. To maximize the coherence of the interferometric pairs, we also introduced a coherence baseline that replaces the time baseline threshold in conventional SBAS-InSAR with the average coherence threshold [37]. This approach allows us to form optimized interferometric pairs, upon which we conduct subsequent SBAS-InSAR processing. A detailed flowchart outlining this process is presented in Figure 2.

The data processing can be summarized into the following steps, according to the flowchart presented in Figure 2:

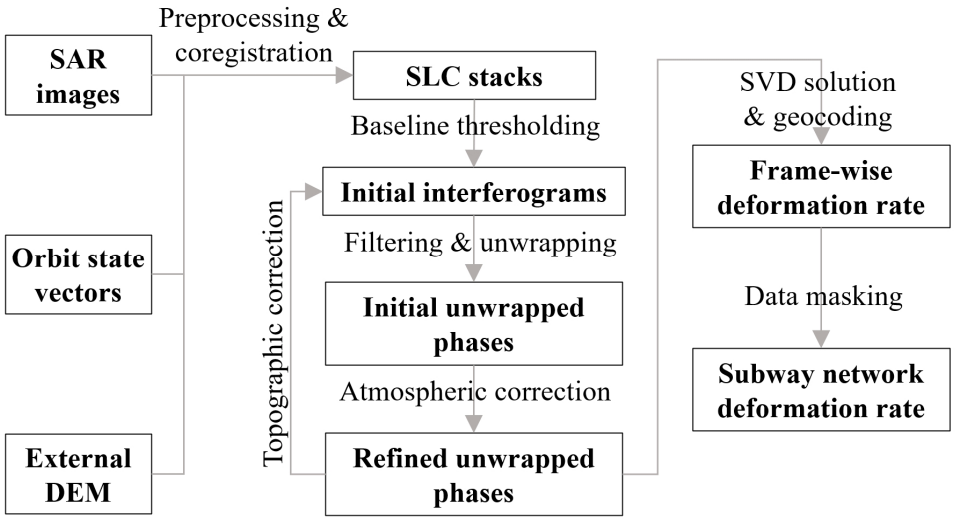

Figure 2. InSAR workflow chart. Abbreviations: DEM, digital elevation model; InSAR, synthetic aperture radar interferometry; SAR, synthetic aperture radar; SLC, single-look complex; and SVD, singular-value decomposition.

Firstly, we prepared various types of data, including SAR data, orbital state vectors, and external digital elevation model (DEM) data. Specifically, we used Shuttle Radar Topography Mission (SRTM) DEM data with a resolution of 30 m. Leveraging these datasets, we embarked on a comprehensive preprocessing and data-registration process. During this phase, we set the multi-look number to 5 × 1 (range × azimuth), resulting in a corresponding ground resolution of 20 m. This enabled us to obtain single-look complex stacks for each image frame, laying a solid foundation for further analysis and deformation extraction.

Then, we selected optimized interferometric pairs based on the average coherence and spatial baseline thresholds. The spatial baseline threshold was set to 50 m. As for the average coherence threshold, there is no unified standard due to significant differences in coherence between Sentinel-1 frames. Next, we ranked the interferometric pairs based on average coherence and selected the top 600 pairs with the best coherence to perform the interferometry, which implies that each Sentinel-1 frame forms 600 interferograms.

After baseline thresholding for a given interferometric pair, assuming that the acquisition time of the reference image is t_A, we deduced that the repeat image is t_B. By performing differential interferometry, filtering, and phase unwrapping for each interferometric pair in sequence to obtain the initial interferograms, the phase value of a certain pixel in the j-th interferogram can be expressed using Equation (1).

$$\delta\varphi_j = \varphi(t_B) - \varphi(t_A) = \frac{4\pi}{\lambda}[d_{t_B} - d_{t_A}] + \delta\varphi_j^{topo} + \delta\varphi_j^{atm} + \delta\varphi_j^{noise} \quad (1)$$

where, $\delta\varphi_j$ is the phase value of a certain pixel in the j-th interferogram. $\varphi(t_B)$ and $\varphi(t_A)$ are the phase value at time t_B and t_A, respectively. λ is the radar wavelength. $\delta\varphi_j^{topo}$, $\delta\varphi_j^{atm}$, and $\delta\varphi_j^{noise}$ represent the contributions of terrain, atmosphere, and noise phase, respectively, among which $\delta\varphi_j^{noise}$ can be effectively reduced in interferograms with good coherence, which is why we adopted the coherence baseline.

To further mitigate topographic and atmospheric errors, we implemented topographic corrections and integrated the corrected topographic phase back to the original interferograms. Following this, we repeated the filtering and atmospheric correction procedures to derive a refined unwrapping phase. We then used the singular-value decomposition method to obtain the minimum norm solution for the deformation rate [36], and performed geocoding to obtain ground deformation rate information in the radar line-of-sight (LOS) direction under geographic coordinates. After obtaining the LOS deformation for each image frame, we invoked a trigonometric function to estimate the vertical displacement by assuming the horizontal deformation was insignificant compared to the vertical deformation, as shown in Equation (2).

$$d_v = d_{LOS}/\cos(\theta) \quad (2)$$

where, d_v and d_{LOS} represent deformations in vertical and LOS directions, respectively, and θ is the radar incidence angle.

After obtaining the ground deformation results for each image frame, we first mosaicked the results of the near-track frames and used the subway network vector to generate masked data with a 250 m buffer zone on both sides of the subway lines. This buffer zone was established to capture any deformation that might occur in the vicinity of the subway network.

Finally, we applied the masking process to the InSAR results, effectively filtering out any deformation data that fell outside the designated subway network and buffer zone. This step allowed us to focus solely on the ground deformation along the subway network, providing us with a clear and concise representation of the deformation patterns within our target area.

3. Results

Figure 3 shows the average annual ground deformation rates from 2018 to 2022 along the subway network, determined through the InSAR process. Overall, the subway network exhibited stability in most cities, with relatively small ground deformations. Nevertheless, certain areas within specific cities, including Beijing, Shanghai, Guangzhou, Shenzhen, Wuhan, Tianjin, Kunming, and Zhengzhou, displayed notable surface deformations. Notably, the maximum deformation rates of multiple cities exceeded −10 mm/year, indicating that they are undergoing more serious ground deformation. Such deformations may be attributed to factors associated with subway construction and operation, which can potentially cause disturbances in the ground. These findings highlight the importance of continuous monitoring and assessment of ground deformation in urban areas, especially around subway networks, to ensure the safety and stability of these critical infrastructures.

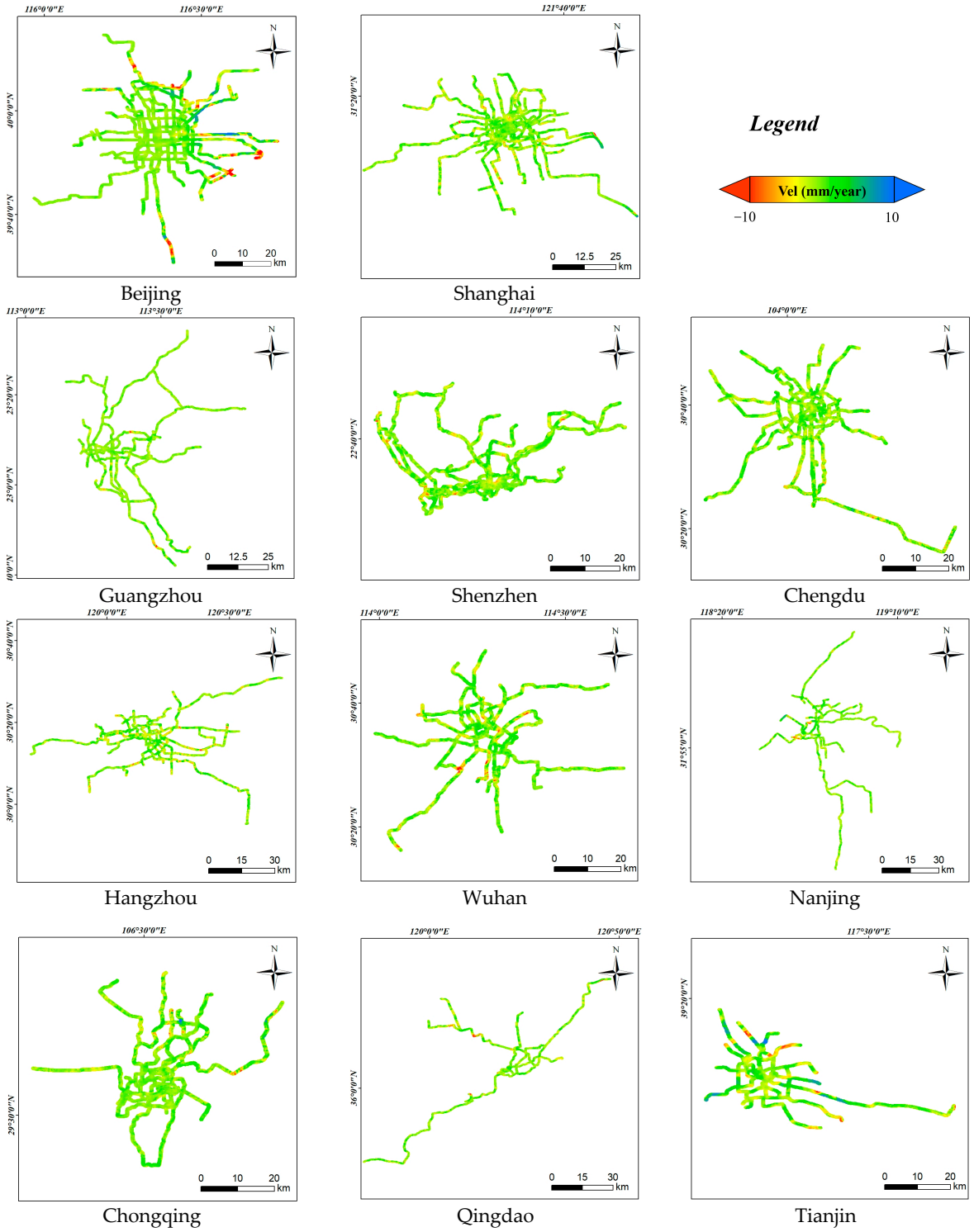

Figure 3. *Cont.*

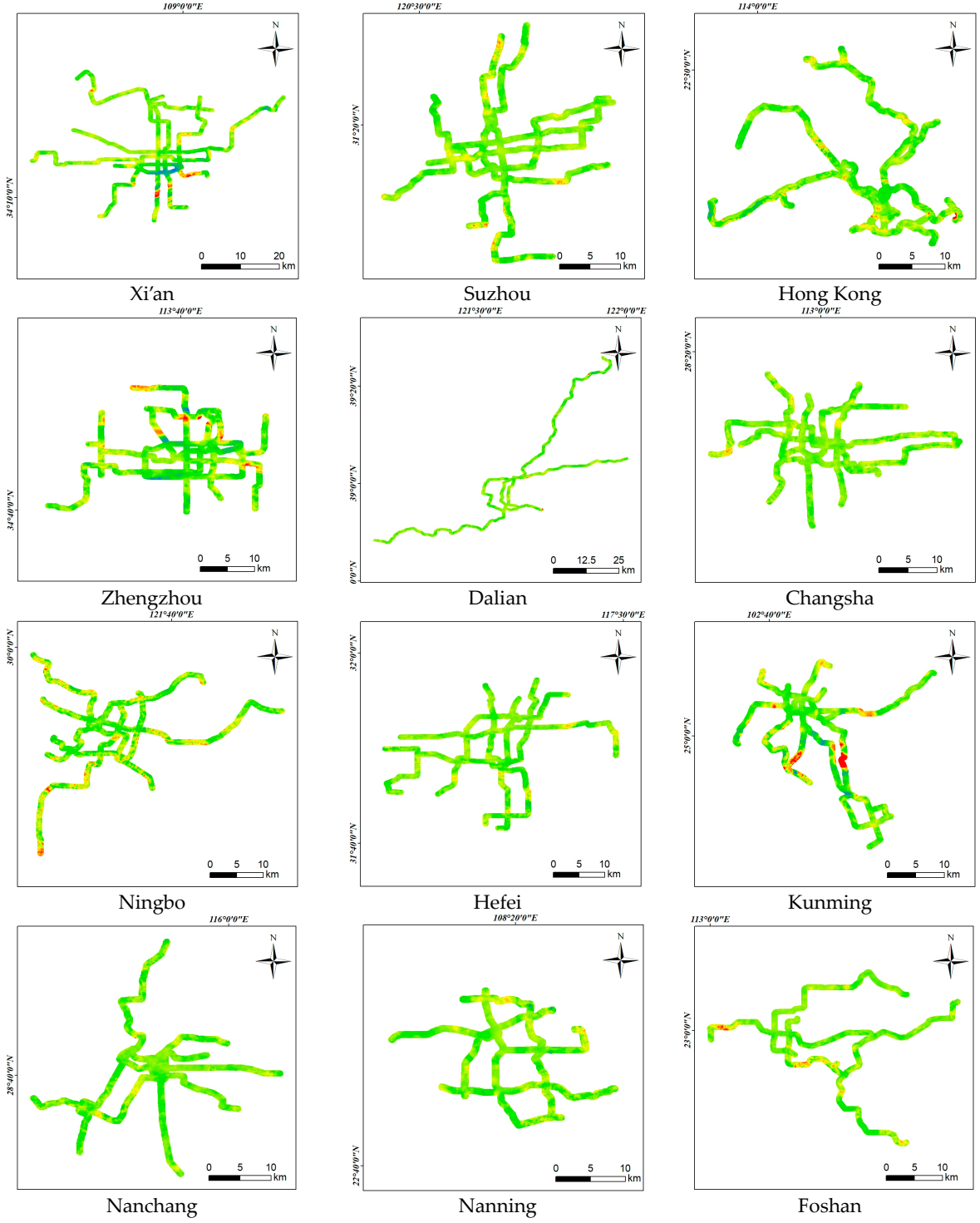

Figure 3. *Cont.*

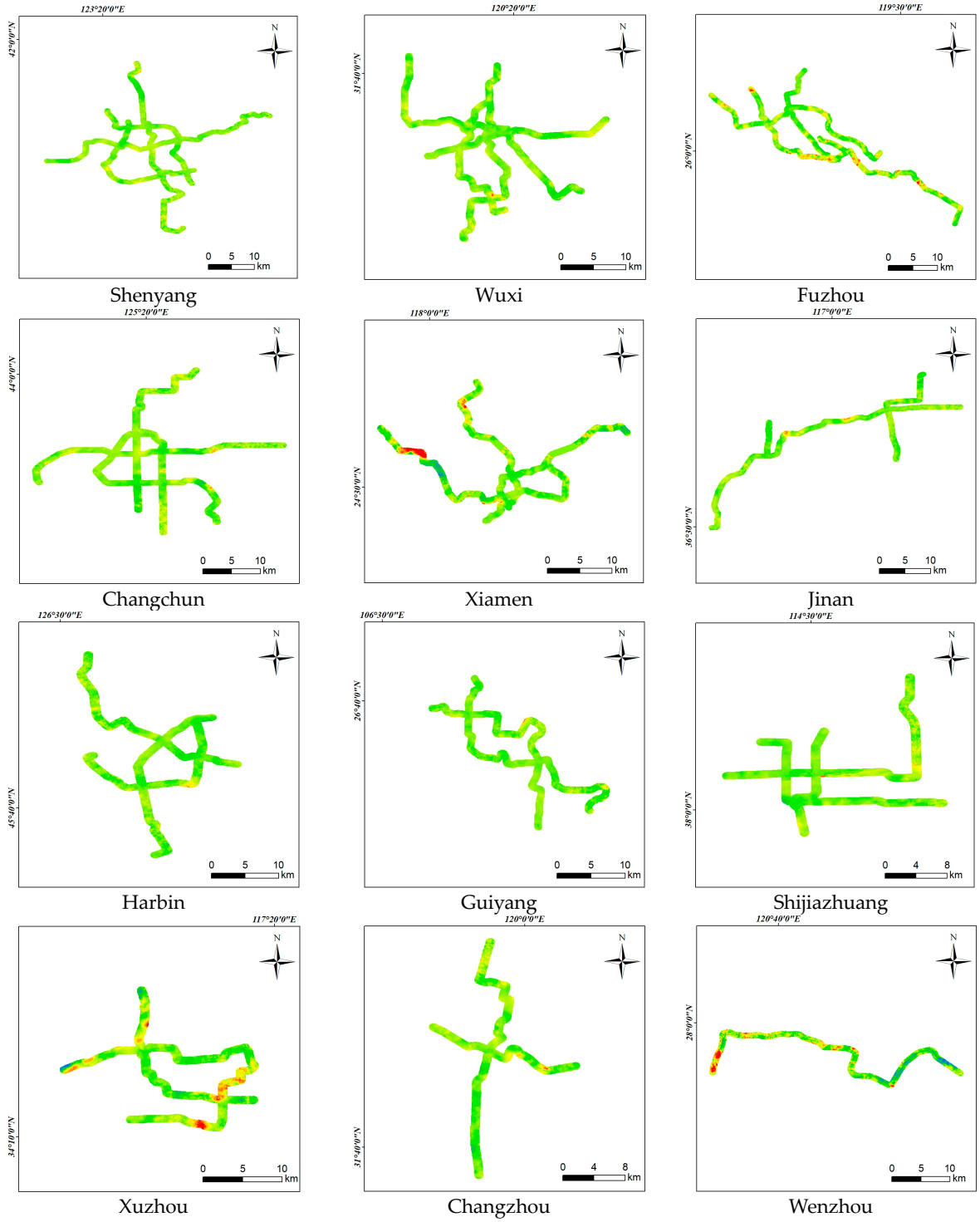

Figure 3. Average annual ground deformation rate maps (2018–2022) for the subway networks of indicated cities.

4. Discussion

We used data measured by continuous GNSS stations as ground truth, to validate the InSAR deformation point that coincides to each GNSS station. Since there are very few GNSS stations distributed above the subway network, we used GNSS station data in all Sentinel-1 frames to expand the validation data scale and improve the reliability of the validation results. A total of 465 GNSS stations participated in the validation, and their distribution is shown in Figure 1. The verification results are shown in Figure 4. The black

dot represents measured GNSS data (horizontal coordinate value) and the InSAR result (vertical coordinate value) of the validation point. The reference red line represents that GNSS data and the InSAR result are equal on this line, with an error of zero. The closer the black dot lies to the reference line, the higher the accuracy of the InSAR result. At the same time, we calculated the RMSE of the InSAR results, which was 3.75 mm/year, quantitatively demonstrating the high accuracy of the InSAR results.

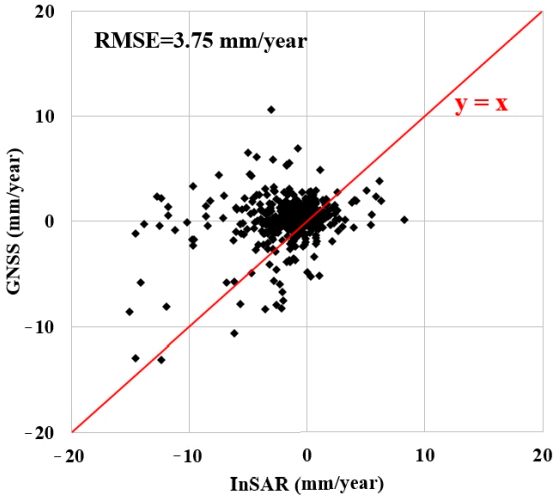

Figure 4. Correlation between the global navigation satellite system (GNSS) and synthetic aperture radar interferometry (InSAR results). Abbreviation: RMSE, root mean square error.

To compare ground deformations along subway networks across different cities, we compiled statistical information from the InSAR deformation results for each city, as summarized in Table 2. Among the 35 cities studied, Beijing stands out with a ground deformation rate of −17.72 mm/year, the highest among all cities. Furthermore, 13 cities exhibited deformation rates exceeding −10 mm/year along their subway networks. These cities include Beijing, Shanghai, Guangzhou, Shenzhen, Hangzhou, Wuhan, Xi'an, Zhengzhou, Dalian, Kunming, Foshan, Fuzhou, and Wenzhou. As evident from the ground deformation rate maps presented in Figure 3, significant surface deformations are apparent along the subway networks in these cities. It is noteworthy that despite the large number of sampling points involved, the mean deformation rate in any of the cities did not exceed ±0.5 mm/year. In addition, the current statistical results indicate that the standard deviation (std) of the ground deformation results along all subway networks did not exceed 3 mm/year.

To assess deformation patterns within subway networks, we established a metric called the subsidence area, which represents the extent of ground that experiences a subsidence rate of less than −5 mm/year. Given that our analysis was grounded on Sentinel-1 data collected over a span of five years, a subsidence rate of less than −5 mm/year translates to a cumulative ground subsidence exceeding 25 mm over this period. Using this threshold, we comprehensively collected data on the number of pixels and the corresponding percentages of subsidence areas for each of the cities we examined (see Table 3).

Table 3 reveals that the subsidence area percentages of Beijing, Tianjin, and Kunming exceed 3%. In Beijing, the subway's subsidence is primarily concentrated in the northern, eastern, and southern regions. Figure 5a–c depict the cumulative deformation curves of representative subsidence zones. Notably, Figure 5a,b show that the cumulative subsidence over the last 5 years exceeded −70 mm. In Tianjin, most subsidence areas are clustered in the north, and Figure 5d–f showcase the typical cumulative deformation curves. The cumulative deformation shown in Figure 5d reached −72 mm. The accelerating downward trends shown in Figure 5e,f for the second half of 2022 (manifesting as significant increases in the slopes of the curves) may have been related to surface disturbances (such as construction) at these locations. Beijing and Tianjin are located in the North China Plain, where surface subsidence is relatively substantial owing to factors such as groundwater extraction,

which also contributes to the seasonal deformation pattern. Since the elevated demand for water during summer months often prompts an increase in groundwater extraction, this in turn can lead to ground subsidence, commonly referred to as "summer subsidence". Conversely, during winter, when water consumption typically decreases, groundwater has a chance to recharge, allowing the ground to partially recover, a process known as "winter rebound". The subway system in Kunming experiences subsidence primarily in its central region. Ground subsidence in this area is relatively severe due to a karst landform, widespread underground rivers, serious groundwater leakage, and disturbances from subway operations. Figure 5g–i show typical cumulative deformation curves of Kunming. Although the deformation curves presented in Figure 5g,h show overall subsidence trends, they all show significant fluctuations and are not obviously related to the season, as seen in Beijing. It is also worth noting that the 5-year cumulative subsidence shown in Figure 5i was close to −100 mm.

Table 2. Deformation statistics of points along the subway network for 35 cities of interest (unit: mm/year).

No.	City	Min	Max	Mean	Std	No.	City	Min	Max	Mean	Std
1	Beijing	−17.72	13.50	0.01	2.32	19	Hefei	−7.80	8.94	0.17	0.73
2	Shanghai	−11.63	5.74	0.02	0.91	20	Kunming	−14.66	5.82	−0.20	1.87
3	Guangzhou	−11.19	5.07	0.06	0.90	21	Nanchang	−7.96	3.52	0.21	0.64
4	Shenzhen	−10.25	9.54	0.04	0.69	22	Nanning	−9.41	5.34	0.13	0.75
5	Chengdu	−8.01	5.27	0.02	0.55	23	Foshan	−13.41	3.30	−0.04	1.16
6	Hangzhou	−10.35	13.22	−0.07	1.04	24	Shenyang	−8.65	5.58	0.03	0.59
7	Wuhan	−12.12	3.50	0.04	1.05	25	Wuxi	−6.55	8.20	0.06	0.65
8	Nanjing	−7.16	5.28	0.14	0.84	26	Fuzhou	−12.19	4.14	−0.13	1.64
9	Chongqing	−7.43	8.35	0.12	0.82	27	Changchun	−7.62	4.60	0.06	0.75
10	Qingdao	−9.57	7.72	−0.02	0.59	28	Xiamen	−7.52	2.91	0.03	0.95
11	Tianjin	−9.13	8.08	−0.35	2.14	29	Jinan	−5.39	4.42	0.07	0.71
12	Xi'an	−14.09	7.79	0.25	1.83	30	Harbin	−7.92	6.74	0.23	0.64
13	Suzhou	−8.02	5.76	0.09	0.77	31	Guiyang	−6.90	2.17	0.17	0.56
14	Hongkong	−9.78	8.61	0.13	0.61	32	Shijiazhuang	−9.26	2.78	−0.07	1.19
15	Zhengzhou	−11.75	5.93	−0.28	1.37	33	Xuzhou	−7.17	9.41	−0.11	0.88
16	Dalian	−10.15	6.71	0.21	0.62	34	Changzhou	−6.73	4.30	0.10	0.65
17	Changsha	−8.47	4.20	0.03	0.61	35	Wenzhou	−13.66	9.78	0.06	2.16
18	Ningbo	−8.27	5.84	−0.08	1.21						

Table 3. Subsidence statistics for the subway systems in 35 cities of interest.

No.	City	Subsidence Area		Regional GDP (Billion RMB)	No.	City	Subsidence Area		Regional GDP (Billion RMB)
		Percentage	Pixel Count				Percentage	Pixel Count	
1	Beijing	3.56	67,186	3743.02	19	Hefei	0.94	4291	1014.08
2	Shanghai	2.84	46,444	4025.37	20	Kunming	5.09	18453	663.61
3	Guangzhou	2.36	27,160	2571.56	21	Nanchang	0.37	1276	629.89
4	Shenzhen	1.56	14,518	2837.44	22	Nanning	0.84	2227	471.98
5	Chengdu	0.29	3020	1816.13	23	Foshan	2.78	8430	1127.17
6	Hangzhou	1.52	18,660	1637.01	24	Shenyang	0.24	910	685.59
7	Wuhan	1.76	17,093	1665.39	25	Wuxi	0.64	1806	1290.31
8	Nanjing	1.76	17,672	1498.64	26	Fuzhou	1.38	3983	1018.04
9	Chongqing	1.77	15,926	2548.85	27	Changchun	0.94	2989	671.31
10	Qingdao	1.23	10,130	1304.01	28	Xiamen	2.20	4567	640.14
11	Tianjin	5.83	41,421	1468.46	29	Jinan	1.52	3160	1018.01
12	Xi'an	1.17	7793	1000.32	30	Harbin	0.43	942	551.51
13	Suzhou	1.84	8978	2093.61	31	Guiyang	0.48	807	435.64
14	Hongkong	1.48	16,701	2422.68	32	Shijiazhuang	2.63	4902	614.22
15	Zhengzhou	2.63	12,962	1187.24	33	Xuzhou	0.71	1155	756.03
16	Dalian	0.61	3348	759.15	34	Changzhou	0.44	557	812.28
17	Changsha	0.85	3649	1239.14	35	Wenzhou	2.41	2974	701.96
18	Ningbo	2.36	9822	1308.78					

Abbreviation: RMB, renminbi.

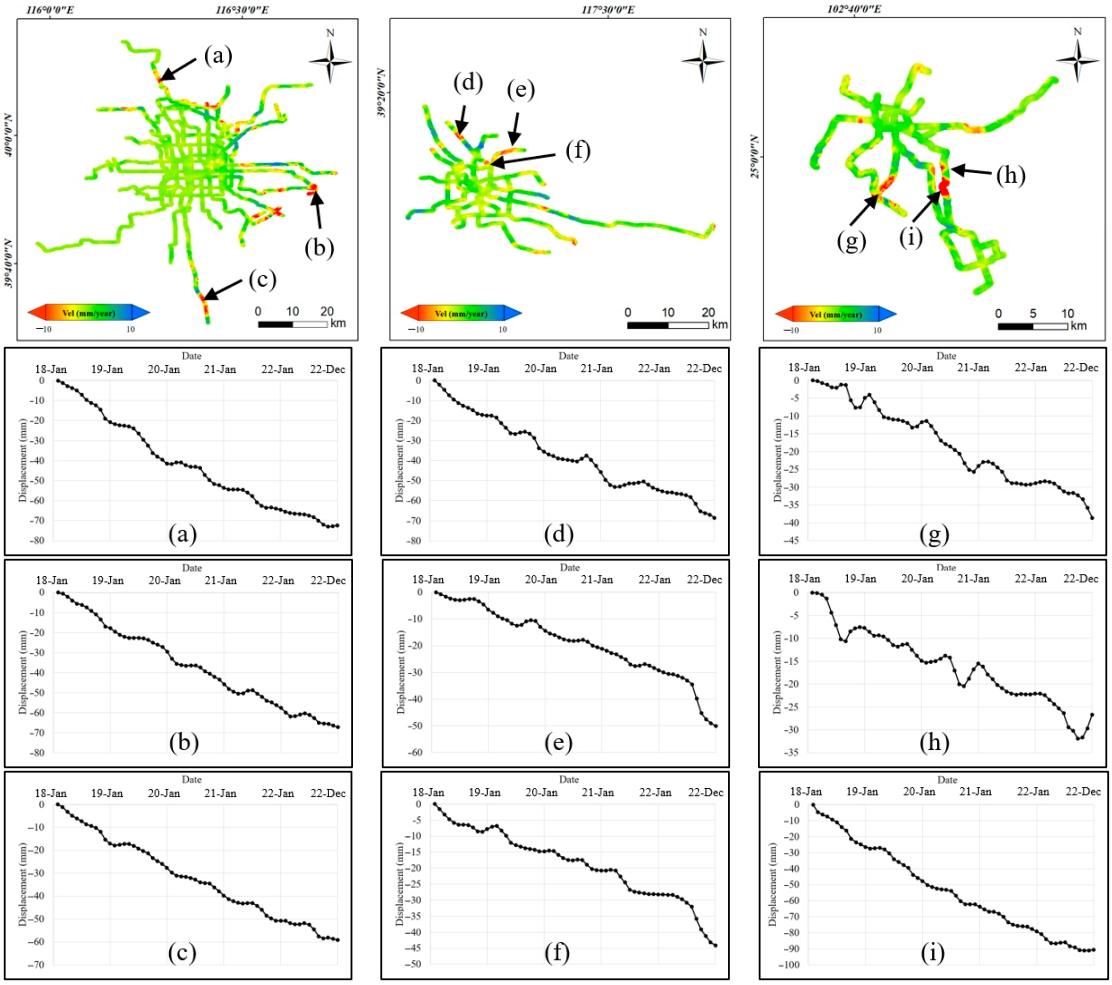

Figure 5. Deformation curves for different locations in China. The cities represented in this figure include Beijing (**a**–**c**), Tianjin (**d**–**f**), and Kunming (**g**–**i**).

Nine cities, including Shanghai, Guangzhou, Suzhou, Zhengzhou, Ningbo, Foshan, Xiamen, Shijiazhuang, and Wenzhou, exhibited deformation area percentages ranging from 2% to 3%. Notably, Shijiazhuang, situated in the North China Plain, underscores the significant ground subsidence observed in several cities within this region. Furthermore, among the twelve cities with deformation area percentages exceeding 2%, seven are coastal cities, accounting for over 58% of the related land. This trend can be attributed to various factors. Coastal cities in China often enjoy policy incentives and convenient transportation, leading to rapid urban development and frequent ground disturbances. Additionally, the increasing population's demands for groundwater resources result in more severe groundwater extraction, further exacerbating ground subsidence. Moreover, subway operations introduce additional disturbances, accelerating the subsidence process. Consequently, coastal cities often experience more severe ground subsidence compared to inland cities.

It is also worth mentioning that although cities like Shenzhen, Hangzhou, Wuhan, Nanjing, Chongqing, Qingdao, and Hong Kong have subsidence area percentages below 2%, the extensive subway networks in these cities result in subsidence areas exceeding 10,000 pixels. Notably, over half of these cities are located in coastal regions, including Shenzhen, Hangzhou, Qingdao, and Hong Kong, further highlighting the challenges faced by coastal urban areas in managing ground subsidence.

To delve deeper into the relationship between urban economic development and subway subsidence, we gathered regional GDP data for the cities of interest spanning

from 2018 to 2022. Based on these data, we computed the average regional GDP for each city over a five-year period, as summarized in Table 3. Subsequently, we employed the Pearson correlation coefficient, a statistical metric ranging from −1 to 1, to assess the link between subway subsidence, specifically measured by the number of pixels in the subsidence area, and the five-year average regional GDP. A positive coefficient indicates a positive correlation, while a negative value signifies a negative correlation. The closer the coefficient is to 1, the stronger the correlation. Using Equation (3), we calculated the Pearson correlation coefficient and discovered a strong correlation of 0.787 between regional GDP and subway subsidence. Figure 6 visually depicts this correlation, providing a clear understanding of the data distribution and the strength of the relationship.

$$\gamma = \frac{cov(x,y)}{\sigma_x \sigma_y} = \frac{\sum_{i=1}^{n}(x_i - \overline{x})(y_i - \overline{y})}{\sqrt{\sum_{i=1}^{n}\left(x_i - \overline{x}\right)^2}\sqrt{\sum_{i=1}^{n}\left(y_i - \overline{y}\right)^2}} \quad (3)$$

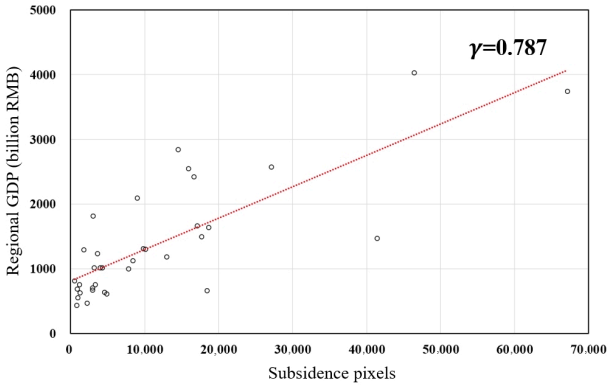

Figure 6. Pearson correlation coefficient between the regional gross domestic product (GDP) and subsidence pixels.

Figure 6 clearly demonstrates a strong positive correlation between a city's regional GDP and the severity of ground subsidence along its subway network. This observation suggests that as a city's economy grows, so does the magnitude of subway-related subsidence. This trend can be attributed to several factors. Firstly, the regional GDP is often indicative of the extent of subway infrastructure within a city. Economically vibrant cities tend to have more extensive and complex subway systems, necessitating frequent maintenance of existing lines and the excavation and construction of new ones. For instance, Beijing boasts 27 subway lines with 12 more under construction, while Shanghai operates 20 lines and has 14 additional ones in the pipeline. The ongoing operation, maintenance, and expansion of these subway networks can disturb the ground surface, making it more vulnerable to subsidence. Moreover, cities with robust economies often attract a higher volume of subway commuters. Beijing and Shanghai, for example, recorded impressive passenger volumes in 2022, with peak daily ridership figures exceeding 13 million. To cater to this significant passenger demand, subway frequencies are increased, which, in turn, can exacerbate disturbances to the ground surface and exacerbate subsidence along subway routes.

Moreover, the construction and operation of subway systems have distinct impacts on various land cover types. To delve deeper into this relationship, we calculated the proportion of different land cover categories within the subsidence zones along the subway networks of all cities under study. We relied on the land cover data of China, provided by the European Space Agency in 2020 with a resolution of 10 m [38]. For statistical analysis, we resampled this data to a 20 m resolution, aligning it with the InSAR results. Subsequently, both datasets were converted into vector format, enabling us to tally the land cover types present within the subsidence areas. The outcomes are presented as percentages in Figure 7.

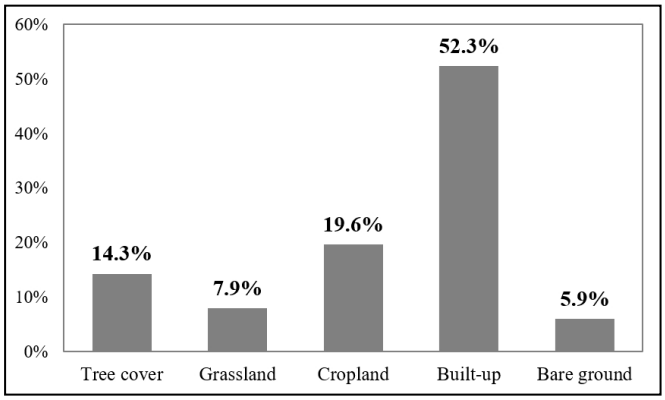

Figure 7. Percentages of different land cover types in different subsidence areas.

Figure 7 shows that the built-up land cover type accounts for the largest proportion among all subsidence areas. This can be attributed to several factors. Firstly, subways are typically constructed in densely populated urban areas, where the geological conditions are often complex, encompassing multiple layers with varying properties such as sand, clay, and rocks. These diverse layers possess differing degrees of stability, leading to a higher susceptibility to ground subsidence. Secondly, the weight of buildings and infrastructure in urban areas exerts significant downward pressure on the Earth's surface, increasing the likelihood of subsidence. Additionally, human activities like commuting, infrastructure development, and groundwater extraction further exacerbate the risk of ground subsidence.

Moreover, Figure 7 indicates that croplands constitute the second largest land cover type affected by subsidence. However, studying deformation in croplands requires careful consideration. The soil in croplands is generally softer, and the vibrations caused by subways can compress the soil particles, leading to subsidence. Furthermore, various disturbance factors, such as crop growth and artificial tillage, are introduced into croplands. These factors may potentially be misinterpreted as ground subsidence signals and should be carefully identified and excluded in future research. The percentages of different land cover types in the subsidence areas follow the order tree cover, grassland, and bare ground. Overall, cultivated land is particularly susceptible to external disturbance factors. In general, it can be concluded that ground subsidence positively correlates with the weight of the land cover. In other words, heavier land cover types exert greater pressure on the surface, resulting in more severe ground subsidence.

5. Conclusions

The construction and operation of subways inevitably cause aboveground disturbances, resulting in deformation. Ground deformation, in turn, impacts the safe operation of subways and the stability of other buildings and facilities on the surface, and monitoring ground deformation along urban subway networks cannot be delayed. Considering the current lack of long-term monitoring results in terms of ground deformation along the entire subway network in China as well as a statistical analysis of the overall deformation states, we extracted ground deformation data for areas along the subway network of 35 major cities in China between 2018 and 2022 with the help of SBAS-InSAR technology and 4705 Sentinel-1 acquisitions. By verifying the results with GNSS data, we found that the RMSE of the InSAR results was 3.75 mm/year, indicating a high accuracy. We also found that the Pearson correlation coefficient between the regional GDP and the ground subsidence along the subway network was 0.787, indicative of a strong positive correlation. Additionally, there is a positive correlation between ground subsidence and the weights of different land cover types.

A statistical analysis of ground deformations along the subway networks in these cities showed that ground subsidence was most prominent along the subway networks in the North China Plain, karst landforms, and coastal areas. Cities such as Beijing, Tianjin,

and Shijiazhuang lie in the North China Plain, and one of the main reasons for their ground subsidence is excessive pumping of groundwater. These areas are densely populated, with developed industry and agriculture, and high levels of water consumption. Long-term overexploitation of groundwater leads to a decrease in groundwater level, which in turn leads to subsidence. A typical city that exhibits Karst landforms is Yunan, where the bedrock is mainly composed of limestone, which has been eroded by groundwater for a long time, forming geological structures such as karst caves and gullies. The existence of these structures makes the ground prone to subsidence when subjected to external forces. In addition, factors such as climate change and precipitation may also affect karst processes, thereby affecting ground stability. In coastal areas such as Guangzhou, Shenzhen, Xiamen, and other cities, the main causes of surface subsidence include seawater intrusion, groundwater exploitation, and the construction of high-rise buildings. The invasion of seawater can alter the physical properties of soil and reduce its bearing capacity; groundwater exploitation can lead to a decrease in groundwater level and cause ground subsidence; the construction of high-rise buildings increases the ground load and exacerbates settlement phenomena. In addition, natural disasters such as storm surges may also pose a threat to the surface stability of coastal areas.

Currently, a summary of the regular deformation characteristics contained in the massive time-series InSAR results obtained in this study is still lacking. Subsequent research will focus on providing a more detailed analysis using large-scale, time-series deformation big data to provide more robust data and support decisions for constructing, operating, and maintaining urban subways.

Author Contributions: Conceptualization, S.W., Z.C. and G.Z.; Funding acquisition, S.W. and Z.C.; Methodology, S.W., Z.C. and Y.Y.; Software, Y.Y.; Validation, S.W., Z.C., G.Z., Z.X. and Y.L.; Writing—original draft, S.W., Z.C., Z.X., Y.L. and Y.Y.; Writing—review and editing, S.W., Z.C., G.Z. and Y.Y. All authors have read and agreed to the published version of the manuscript.

Funding: This work was supported by the National Natural Science Foundation of China projects (NSFC) (grant number 41801397), the National Key Research and Development Program of China (grant number 2021YFB3900604), and the PhD Special Project of Nanyang Normal University (grant number 231384).

Data Availability Statement: Senitnel-1 SAR data were downloaded from https://scihub.copernicus.eu/, accessed on 15 January 2023; orbit state data were downloaded from https://s1qc.asf.alaska.edu/aux_poeorb/, accessed on 10 January 2023; and SRTM DEM data were downloaded from https://asf.alaska.edu/, accessed on 7 January 2023.

Acknowledgments: The authors would like to thank the European Space Agency for providing the Sentinel-1 data and Qianxun SI for providing the GNSS data.

Conflicts of Interest: The authors declare no conflicts of interest.

References

1. Cai, Z.; Wang, J.; Li, T.; Yang, B.; Su, X.; Guo, L.; Ding, Z. A novel trajectory based prediction method for urban subway design. *ISPRS Int. J. Geoinf.* **2022**, *11*, 126. [CrossRef]
2. Yang, J.; Chen, S.; Qin, P.; Lu, F. The Effects of Subway Expansion on Traffic Conditions: Evidence from Beijing. Environmental Development Discussion Paper Serier EfD DP. 2015, pp. 15–22. Available online: https://www.rff.org/publications/working-papers/the-effects-of-subway-expansion-on-traffic-conditions-evidence-from-beijing/ (accessed on 4 February 2023).
3. Xiao, D.; Li, B.; Cheng, S. The effect of subway development on air pollution: Evidence from China. *J. Clean. Prod.* **2020**, *275*, 124149. [CrossRef]
4. Hu, C.; Cai, D.; Wen, Y. Does subway mileage affect urban housing prices? An economic growth perspective. *Appl. Econ.* **2023**, 1–13. [CrossRef]
5. Ma, P.; Zhang, Y.; Zhang, Z.; Wu, Z.; Yu, C. Building risk monitoring and prediction using integrated multi-temporal InSAR and numerical modeling techniques. *Int. J Appl. Earth Obs.* **2022**, *114*, 103076. [CrossRef]
6. Galloway, D.; Burbey, T. Review: Regional land subsidence accompanying groundwater extraction. *Hydrogeol. J.* **2011**, *19*, 1459–1486. [CrossRef]
7. Liu, Y.; Qiu, H.; Kamp, U.; Wang, N.; Wang, J.; Huang, C.; Tang, B. Higher temperature sensitivity of retrogressive thaw slump activity in the Arctic compared to the Third Pole. *Sci. Total Environ.* **2024**, *914*, 170007. [CrossRef] [PubMed]

8. Chen, W.; Gong, H.; Chen, B.; Liu, K.; Gao, M.; Zhou, C. Spatiotemporal evolution of land subsidence around a subway using InSAR time-series and the entropy method. *GISci. Remote Sens.* **2017**, *54*, 78–94. [CrossRef]
9. Wang, R.; Yang, M.; Dong, J.; Liao, M. Investigating deformation along metro lines in coastal cities considering different structures with InSAR and SBM analyses. *Int. J. Appl. Earth Obs. Geoinf.* **2022**, *115*, 103099. [CrossRef]
10. Wu, Z.; Ma, P.; Zheng, Y.; Gu, F.; Liu, L.; Lin, H. Automatic detection and classification of land subsidence in deltaic metropolitan areas using distributed scatterer InSAR and oriented R-CNN. *Remote Sens. Environ.* **2023**, *290*, 113545. [CrossRef]
11. Richard, B.; Philipp, H. Synthetic aperture radar interferometry. *Inverse Probl.* **1998**, *14*, R1. [CrossRef]
12. Wright, T.J.; Parsons, B.E.; Lu, Z. Toward mapping surface deformation in three dimensions using InSAR. *Geophys. Res. Lett.* **2004**, *31*, 169–178. [CrossRef]
13. Chen, F.; Xu, H.; Zhou, W.; Zheng, W.; Deng, Y.; Parcharidis, I. Three-dimensional deformation monitoring and simulations for the preventive conservation of architectural heritage: A case study of the Angkor Wat Temple, Cambodia. *GISci. Remote Sens.* **2021**, *58*, 217–234. [CrossRef]
14. Hooper, A.; Zebker, H.; Segall, P.; Kampes, B. A New Method for Measuring Deformation on Volcanoes and Other Natural Terrains Using Insar Persistent Scatterers. *Geophys. Res. Lett.* **2004**, *31*, 96–106. [CrossRef]
15. Ye, B.; Qiu, H.; Tang, B.; Liu, Y.; Liu, Z.; Jiang, X.; Yang, D.; Ullah, M.; Zhu, Y.; Kamp, U. Creep deformation monitoring of landslides in a reservoir area. *J. Hydrol.* **2024**, *632*, 130905. [CrossRef]
16. Wasowski, J.; Bovenga, F. Investigating landslides and unstable slopes with satellite Multi Temporal Interferometry: Current issues and future perspectives. *Eng. Geol.* **2014**, *174*, 103–138. [CrossRef]
17. Dong, J.; Lai, S.; Wang, N.; Wang, Y.; Zhang, L.; Liao, M. Multi-scale deformation monitoring with Sentinel-1 InSAR analyses along the Middle Route of the South-North Water Diversion Project in China. *Int. J. Appl. Earth Obs. Geoinf.* **2021**, *100*, 102324. [CrossRef]
18. Li, Z.; Zhu, W.; Yu, C.; Zhang, Q.; Zhang, C.; Liu, Z.; Zhang, X.; Chen, B.; Du, J.; Song, C.; et al. Interferometric synthetic aperture radar for deformation mapping: Opportunities, challenges and the outlook. *Acta Geod. Cartogr. Sin.* **2022**, *51*, 1485–1519.
19. Barra, A.; Solari, L.; Béjar-Pizarro, M.; Monserrat, O.; Bianchini, S.; Herrera, G.; Crosetto, M.; Sarro, R.; González-Alonso, E.; Mateos, R.M.; et al. A Methodology to Detect and Update Active Deformation Areas Based on Sentinel-1 SAR Images. *Remote Sens.* **2017**, *9*, 1002. [CrossRef]
20. Hamling, I.J.; Hreinsdóttir, S.; Clark, K.; Elliott, J.; Liang, C.; Fielding, E.; Litchfield, N.; Villamor, P.; Wallace, L.; Wright, T.J. Complex multifault rupture during the 2016 M w 7.8 Kaikōura earthquake, New Zealand. *Science* **2017**, *356*, eaam7194. [CrossRef]
21. Fadhillah, F.; Chmad, A.R.; Lee, C.W. Integration of InSAR timeseries data and GIS to assess land subsidence along subway lines in the Seoul metropolitan area South Korea. *Remote Sens.* **2020**, *12*, 3505. [CrossRef]
22. Espiritu, K.W.; Reyes, C.J.; Benitez, T.M.; Tokita, R.C.; Galvez, L.J.; Ramirez, R. Sentinel-1 interferometric synthetic aperture radar (InSAR) reveals continued ground deformation in and around Metro Manila, Philippines, associated with groundwater exploitation. *Nat. Hazards* **2022**, *114*, 3139–3161. [CrossRef]
23. Gheorghe, M.; Armaș, I.; Dumitru, P.; Călin, A.; Bădescu, O.; Necsoiu, M. Monitoring subway construction using Sentinel-1 data: A case study in Bucharest, Romania. *Int. J. Remote Sens.* **2020**, *41*, 2644–2663. [CrossRef]
24. Duan, L.; Gong, H.; Chen, B.; Zhou, C.; Lei, K.; Gao, M.; Yu, H.; Cao, Q.; Cao, J. An improved multi-sensor MTI time-series fusion method to monitor the subsidence of Beijing subway network during the past 15 years. *Remote Sens.* **2020**, *12*, 2125. [CrossRef]
25. Dong, S.; Samsonov, S.; Yin, H.; Ye, S.; Cao, Y. Time-series analysis of subsidence associated with rapid urbanization in Shanghai, China measured with SBAS InSAR method. *Environ. Earth Sci.* **2014**, *72*, 677–691. [CrossRef]
26. Perissin, D.; Wang, Z.; Lin, H. Shanghai subway tunnels and highways monitoring through Cosmo-SkyMed persistent scatterers. *ISPRS J. Photogram. Remote Sens.* **2012**, *73*, 58–67. [CrossRef]
27. Zhang, J.; Ke, C.; Shen, X.; Lin, J.; Wang, R. Monitoring land subsidence along the subways in Shanghai on the basis of time-series InSAR. *Remote Sens.* **2023**, *15*, 908. [CrossRef]
28. Yuan, Y.; Qin, Y.; Zhang, Y.; Xie, L.; Meng, X.; Guo, Z. Environmental risk source analysis and classification of zones: Subway construction. *Appl. Sci.* **2023**, *13*, 5831. [CrossRef]
29. Xu, X.; Zhao, D.; Ma, C.; Lian, D. Monitoring subsidence deformation of Suzhou subway using InSAR timeseries analysis. *IEEE Access* **2021**, *9*, 3400–3416. [CrossRef]
30. Tao, Q.; Guo, Z.; Wang, F.; An, Q.; Han, Y. SBAS-InSAR time series ground subsidence monitoring along Metro Line 13 in Qingdao, China. *Arab. J. Geosci.* **2021**, *14*, 2628. [CrossRef]
31. Zheng, M.; Guo, Q.; Zhao, R.; Wang, L.; Han, Y. Surface subsidence disasters over Xuzhou city, China 2014–2018 revealed by InSAR and Peck model. *Environ. Earth Sci.* **2023**, *82*, 264. [CrossRef]
32. Hu, B.; Li, Z. Time-series InSAR technology for ascending and descending orbital images to monitor surface deformation of the metro network in Chengdu. *IEEE J. Sel. Top. Appl. Earth Obs. Remote Sens.* **2021**, *14*, 12583–12597. [CrossRef]
33. Gao, H.; Xiong, L.; Chen, J.; Lin, H.; Feng, G. Surface Subsidence of Nanchang, China 2015–2021 Retrieved via Multi-Temporal InSAR Based on Long- and Short-Time Baseline Net. *Remote Sens.* **2023**, *15*, 3253. [CrossRef]
34. Zhao, S.; Li, P.; Li, H.; Zhang, T.; Wang, B. Monitoring and Comparative Analysis of Hohhot Subway Subsidence Using StaMPS-PS Based on Two DEMS. *Remote Sens.* **2023**, *15*, 4011. [CrossRef]
35. Ministry of Transport of People's Republic of China. Urban Rail Transit Operation Data Report. 2022. Available online: https://www.gov.cn/xinwen/2023-01/20/content_5738226.htm (accessed on 15 November 2023). (In Chinese)

36. Berardino, P.; Fornaro, G.; Lanari, R.; Sansoti, E. A new algorithm for surface deformation monitoring based on small baseline differential SAR interferograms. *IEEE Trans. Geosci. Remote Sens.* **2002**, *40*, 2375–2383. [CrossRef]
37. Wang, S.; Zhang, G.; Chen, Z.; Cui, H.; Zheng, Y.; Xu, Z.; Li, Q. Surface deformation extraction from small baseline subset synthetic aperture radar interferometry (SBAS-InSAR) using coherence-optimized baseline combinations. *GISci. Remote Sens.* **2022**, *59*, 295–309. [CrossRef]
38. Buchhorn, M.; Lesiv, M.; Tsendbazar, N.-E.; Herold, M.; Bertels, L.; Smets, B. Copernicus Global Land Cover Layers—Collection 2. *Remote Sens.* **2020**, *12*, 1044. [CrossRef]

Disclaimer/Publisher's Note: The statements, opinions and data contained in all publications are solely those of the individual author(s) and contributor(s) and not of MDPI and/or the editor(s). MDPI and/or the editor(s) disclaim responsibility for any injury to people or property resulting from any ideas, methods, instructions or products referred to in the content.